RSC Advances

PAPER

View Article Online
View Journal | View Issue

Cite this: *RSC Adv.*, 2023, **13**, 14139

Electrochemical capacitance properties of pre-sodiated manganese oxide for aqueous Na-ion supercapacitors†

Aneesh Anand Nechikott and Prasant Kumar Nayak *

Mn-based oxides are widely investigated as electrode materials for electrochemical supercapacitors, because of their high specific capacitance in addition to the high abundance, low cost, and environmental friendliness of Mn. The pre-insertion of alkali metal ions is found to improve the capacitance properties of MnO_2. While the capacitance properties of MnO_2, Mn_2O_3, P2-$Na_{0.5}MnO_2$, and O3-$NaMnO_2$ *etc.* are reported, there is no report yet on the capacitive performance of P2-$Na_{2/3}MnO_2$, which has already been studied as a potential positive electrode material for Na-ion batteries. In this work, we have synthesized sodiated manganese oxide, P2-$Na_{2/3}MnO_2$ by a hydrothermal method followed by annealing at a high temperature of about 900 °C for 12 h. For comparison, manganese oxide Mn_2O_3 (without pre-sodiation) is synthesized by following the same method, but annealing at 400 °C. While P2-$Na_{2/3}MnO_2$ exhibits a high specific capacitance of 234 F g^{-1}, Mn_2O_3 can deliver only 115 F g^{-1} when cycled at 0.4 A g^{-1} in an aqueous electrolyte of 1.0 M Na_2SO_4 in a three-electrode cell. An asymmetric supercapacitor $Na_{2/3}MnO_2$||AC is assembled, which can exhibit a SC of 37.7 F g^{-1} at 0.1 A g^{-1} with an energy density of 20.9 W h kg^{-1}, based on the total weight of $Na_{2/3}MnO_2$ and AC with an operational voltage of 2.0 V and possesses excellent cycling stability. This asymmetric $Na_{2/3}MnO_2$||AC supercapacitor can be cost-effective considering the high abundance, low-cost and environmental friendliness of Mn-based oxides and aqueous Na_2SO_4 electrolyte.

Received 13th March 2023
Accepted 30th April 2023

DOI: 10.1039/d3ra01657a

rsc.li/rsc-advances

1. Introduction

There is growing research interest in electrochemical supercapacitors because of their high-power density and long cycle-life.[1–6] While batteries possess high energy density (>50 W h kg^{-1}), conventional capacitors exhibit a high-power density of 10^3 kW kg^{-1}. Electrochemical supercapacitors possessing intermediate energy density (5–10 W h kg^{-1}) and power density (>10^3 W kg^{-1}) bridge the gap between them.[1,6] Currently, aqueous Zn-ion hybrid capacitors and batteries with higher energy to power ratio find great potential to overcome the low energy density of aqueous supercapacitors.[7,8] While supercapacitors can find many applications, these can be used complementary to batteries in electric vehicles where they can withstand high pulse power. Depending on the charge storage mechanism, there are two types of supercapacitors, namely electrical double-layer capacitors, where the capacitance arises due to the physisorption of ions from/to the electrode, and pseudo-capacitors involving the Faradaic redox reaction of active material.[9–11] The double-layer capacitance of activated carbon (AC) is limited to 100–250 F g^{-1} depending on the surface area of the AC sample as well as the electrolyte used.[12,13] Pseudo-capacitances of transition metal oxides are found to be higher than the double-layer SC of AC. Among transition metal oxides, RuO_2 is a promising electrode material, because of its high SC of 700–800 F g^{-1}.[14–17] However, low-cost and environment-friendly metal oxides such as MnO_2, NiO, $Ni(OH)_2$, $NiCo_2O_4$ are widely studied as alternatives to toxic and costly RuO_2.[18–27] For example, Munawar *et al.* synthesized flower-like NiO by a surfactant-assisted method, which exhibited a SC of 397 F g^{-1} at a specific current of 1 A g^{-1}.[26] Recently, Yewale *et al.* synthesized plate-like $NiCo_2O_4$ by a hydrothermal method, which exhibited a SC of 550 F g^{-1}.[27] Also, there is growing interest on transition metal sulfides such as $CuCo_2S_4$, Co_3S_4, $NiCo_2S_4$ *etc.*, because of their high specific capacitance values.[28–31] Abuali *et al.* synthesized $CuCo_2S_4$ nanoparticles in polyaniline hollow spheres, which can exhibit a SC of 1120 F g^{-1} at a specific current of 1 A g^{-1}.[29] However, these materials exhibit their capacitance properties in alkali solutions, which are not environmentally friendly.

Mn-based cheap oxides can exhibit SC of 150–300 F g^{-1} depending on the crystallographic form, morphology and the nature of the aqueous electrolyte used. The pre-insertion of alkali metal ions (Na^+, K^+) is found to influence the capacitance

Materials Electrochemistry Research Laboratory, Department of Chemistry, SRM Institute of Science and Technology, Kattankulathur-603203, India. E-mail: prasantn1@srmist.edu.in

† Electronic supplementary information (ESI) available. See DOI: https://doi.org/10.1039/d3ra01657a

properties of MnO_2.[32,33] While the capacitance properties of MnO_2, $Na_{0.21}MnO_2$, $Na_{0.5}MnO_2$, and $NaMnO_2$ *etc.* are well studied and reported, the performance of P2-$Na_{2/3}MnO_2$ (which has been investigated as a potential positive electrode material for Na-ion batteries) is not yet studied. The capacitive performance of MnO_2 and alkali metal ion pre-inserted MnO_2 are listed along with our current work in Table 1.[32–42]

The energy density of supercapacitors depends on the specific capacitance of electrode materials and the operating voltage that depends on the stability of the electrolyte. Based on the electrode materials used, there are two types of supercapacitors, namely symmetric as well as asymmetric supercapacitors. The symmetric supercapacitors involving two similar electrodes possess limited energy density due to low operational voltage in aqueous electrolytes. However, asymmetric supercapacitors employing two different types of electrodes can be operated with a higher voltage, thus increasing their energy density as compared to symmetric supercapacitors. Among various asymmetric supercapacitors, MnO_2||AC,[43–47] $NaMnO_2$||AC,[34–36,48] and $NiCoO_2$||AC[49–52] are reported to exhibit energy density of 10–30 W h kg^{-1}. Asymmetric supercapacitors based on MnO_2||AC use mostly amorphous MnO_2, which does not exhibit good cycling performance. Layered sodiated transition metal oxides are classified as O3 and P2-type depending on the site which Na occupies. P2-$Na_{2/3}MnO_2$ is widely studied as a positive electrode material for rechargeable Na-ion batteries.[53–56] Although the electrochemical performance of O3-type $NaMnO_2$ and P2-type $Na_{0.21}MnO_2$ and $Na_{0.5}MnO_2$ for supercapacitor studies is reported, to the best of the authors' knowledge the electrochemical performance of P2-$Na_{2/3}MnO_2$ as a pseudo-capacitive electrode material is not yet evaluated.

In this work, we have synthesized P2-$Na_{2/3}MnO_2$ by a hydrothermal method followed by annealing at 900 °C for 12 h. In order to emphasize the importance of pre-sodiation, manganese oxide without pre-sodiation is synthesized by the same hydrothermal method and then annealing at 400 °C. We have systematically investigated the electrochemical capacitive performance of both materials by cyclic voltammetry and charge–discharge cycling. While P2-$Na_{2/3}MnO_2$ exhibits a SC of 234 F g^{-1}, Mn_2O_3 can deliver only 115 F g^{-1} when cycled at 0.4 A g^{-1} in 1.0 M Na_2SO_4 electrolyte with good cycling stability over 4000 cycles. Finally, an asymmetric $Na_{2/3}MnO_2$||AC supercapacitor is assembled using $Na_{2/3}MnO_2$ as a positive and activated carbon as a negative electrode in an aqueous electrolyte of 1.0 M Na_2SO_4, which exhibits a SC of 37.7 F g^{-1} within 2.0 V operating voltage with excellent cycling stability over 6000 cycles.

2. Materials and methods

2.1 Materials used

Analytical grade chemicals such as manganese nitrate, sodium nitrate, urea, *N*-methyl-2-pyrrolidinone (NMP), poly(vinylidene fluoride) (PVDF), commercial activated carbon (AC) powder and sodium sulphate were used as received. Double distilled (DD) water was used to dissolve the metal salts and urea.

2.2 Methods

2.2.1 Synthesis and characterization of $Na_{2/3}MnO_2$. P2-type $Na_{2/3}MnO_2$ was synthesized by a hydrothermal method followed by annealing at 900 °C for 12 h. In a typical preparation, 5.020 g of manganese nitrate and 1.071 g of $NaNO_3$ were dissolved in 40 ml of DD water with stirring. Another solution containing urea was added dropwise to this solution with continuous stirring for 2 h. Then, the solution was transferred to a Teflon-lined stainless-steel autoclave, which is then heated at 150 °C for 12 h. The precipitate was filtered upon cooling to room temperature and dried, which was then heated at 500 °C for 3 h. The obtained sample was ground to powder form and then annealed at 900 °C for 12 h. Mn_2O_3 was synthesized from manganese nitrate and urea by following the same procedure, however, annealed at 400 °C. The obtained powder samples ware characterized using a Bruker Advance 8 powder X-ray diffractometer (XRD) with monochromatized Cu Kα radiation ($\lambda = 1.54056$ Å). The morphology of both samples was examined by scanning electron microscopy (SEM) (FEI, Quanta 200). The transmission electron microscopy (TEM) analysis was performed using a JEM-2100 plus Microscope JEOL (Japan).

2.2.2 Electrode preparation and electrochemical measurements. The active mass (75 wt%) was mixed with 15 wt% of

Table 1 Specific capacitances of Mn-based oxides in an aqueous Na_2SO_4 electrolyte

Electrode material	Electrolyte	Potential	Specific capacitance	Reference
Mesoporous MnO_2	0.1 M Na_2SO_4	0–1.0 V	190 F g^{-1} (1 A g^{-1})	37
Mesoporous MnO_2	0.1 M $Ca(NO_3)_2$	0–1.0	240 F g^{-1} (1.0 A g^{-1})	38
α-MnO_2	0.1 M Na_2SO_4	0–1.0 V	166 F g^{-1} (0.2 A g^{-1})	39
δ-MnO_2	1.0 M Na_2SO_4	0–1.0 V	210 F g^{-1} (0.3 A g^{-1})	40
MnO_2 nano wire	0.1 M Na_2SO_4	0–0.9 V	350 F g^{-1} (0.1 mA cm^{-2})	41
β-MnO_2 nano wire	1.0 M Na_2SO_4	0–0.8 V	453 F g^{-1} (0.5 A g^{-1})	42
$K_{0.6}MnO_2$	1.0 M KTFSI	0–1.2 V	254 F g^{-1} (1.0 A g^{-1})	32
$Na_{0.5}MnO_2$	1.0 M Na_2SO_4	0–1.2 V	287 F g^{-1} (1.0 A g^{-1})	33
$Na_{0.21}MnO_2$	0.5 M Na_2SO_4	0–1.3 V	184 F g^{-1} (3.0 A g^{-1})	34
$Na_{0.35}MnO_2$	0.5 M Na_2SO_4	0–1.0 V	157 F g^{-1} (0.2 A g^{-1})	35
$Na_{0.95}MnO_2$	0.5 M Na_2SO_4	0–1.0 V	95 F g^{-1} (0.2 A g^{-1})	35
$NaMnO_2$	0.5 M Na_2SO_4	0–1.1 V	140 F g^{-1} (1.0 A g^{-1})	36
$Na_{2/3}MnO_2$	**1.0 M Na_2SO_4**	**−0.2–1.2 V**	**234 F g^{-1} (0.4 A g^{-1})**	**This work**

conductive super P carbon and 10 wt% of PVDF binder and ground in a mortar. A few drops of *N*-methyl-2-pyrrolidinone (NMP) solvent were added to the mixture and ground to obtain a homogeneous slurry. For preparing the AC electrode, the proportion of active mass, super P carbon and PVDF was 80 : 10 : 10 by wt%. Electrodes were prepared by repeated brush coating onto graphite foil current collectors (0.30 μm thick) and drying to get the desired mass. The electrodes were finally dried

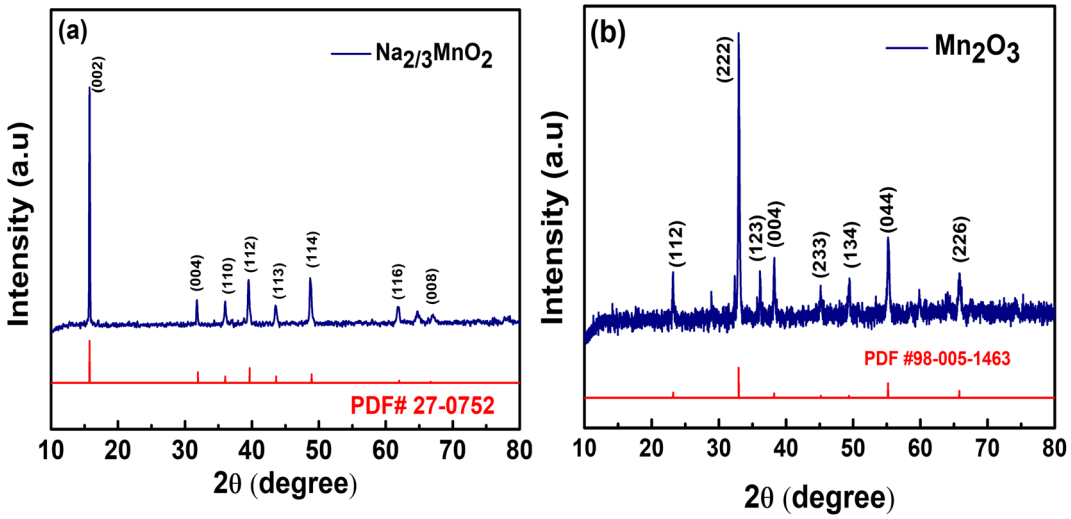

Fig. 1 XRD patterns of (a) $Na_{2/3}MnO_2$, (b) Mn_2O_3 synthesized by hydrothermal method followed by annealing.

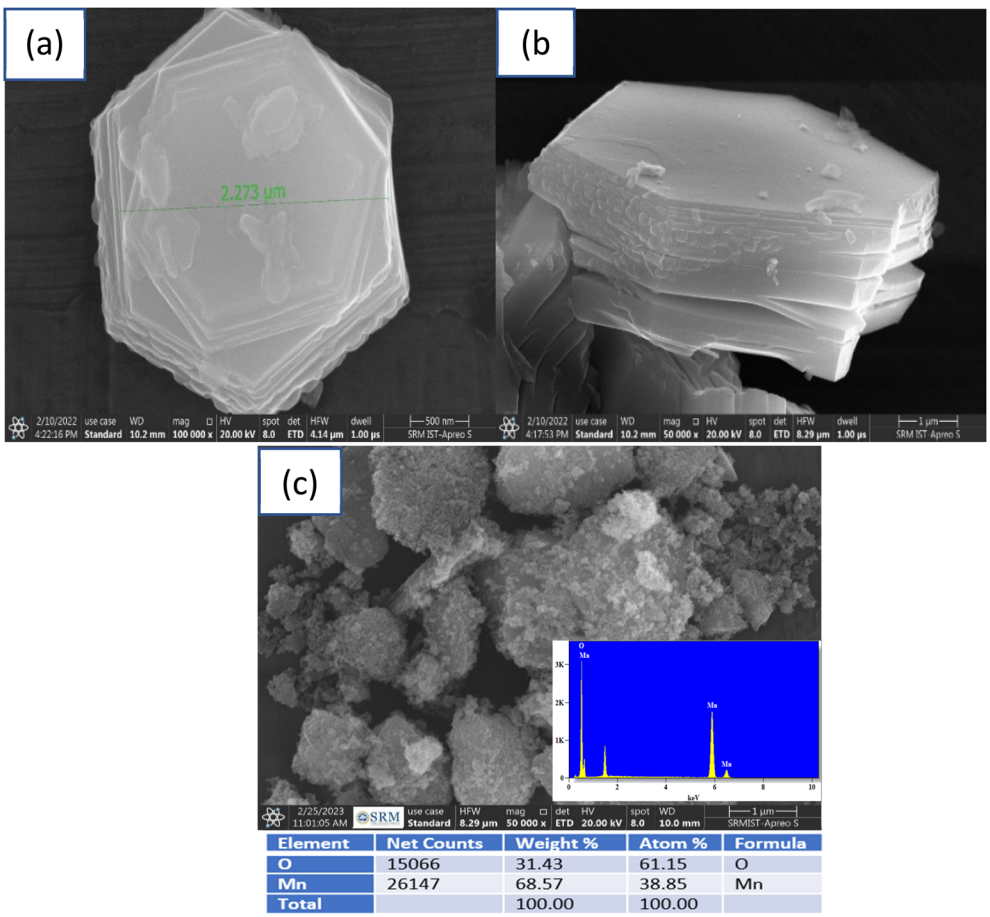

Element	Net Counts	Weight %	Atom %	Formula
O	15066	31.43	61.15	O
Mn	26147	68.57	38.85	Mn
Total		100.00	100.00	

Fig. 2 SEM images (a) top view and (b) side view of $Na_{2/3}MnO_2$ and (c) Mn_2O_3 synthesized by hydrothermal method followed by annealing.

at 100 °C for 6 h in a vacuum oven before assembling for their electrochemical testing. The electrode area was 1.0 cm^2 and the loading of the active mass was 1.0 mg cm^{-2}. The cyclic voltammetry (CV) and galvanostatic charge–discharge (GCD) tests of individual electrodes were performed using a three-electrode cell using Pt foil and saturated calomel electrode (SCE) as counter and reference electrodes, respectively, in an aqueous solution of 1.0 M Na_2SO_4. The experimental results such as the specific capacitance of the $Na_{2/3}MnO_2$ and Mn_2O_3 are reported here after performing the experiments for at least 2–3 times. The experimental error is within 2–4%. The asymmetric $Na_{2/3}MnO_2$||AC supercapacitor was assembled using 4 cm × 4 cm electrodes with a commercial cellulose acetate membrane as the separator and tested in a two-electrode cell using an aqueous electrolyte solution of 1.0 M Na_2SO_4. The electrochemical impedance spectra (EIS) were measured at open circuit potential (OCP) with an AC amplitude of 10 mV in the frequency range of 10 kHz to 0.01 Hz using ZIVE SP1 potentiostat/galvanostat.

3. Results and discussion

The XRD pattern measured for the synthesized $Na_{2/3}MnO_2$ powder material (Fig. 1a) matched well with the reported pattern (JCPDF 27-0751).[57,58] The XRD peaks at 2θ of 15.8°, 31.83°, 36.29°, 39.63°, 43.62°, 48.72°, 61.95°, 64.73° and 67.09° correspond to (002), (004), (100), (102), (103), (104), (106), (110) and (008), respectively. $Na_{2/3}MnO_2$ crystallizes in hexagonal $P6_3/mmc$ space group. The alkali Na^+ cation occupies the trigonal prismatic site and is sandwiched between the MO_2 sheets. The lattice parameters analyzed with Xpert High score are found to be $a = b = 2.8802$ Å, $c = 11.264$ Å with cell volume of 80.93 $Å^3$. The XRD pattern of Mn_2O_3 is matching well with the reported pattern (JCPDF 98-005-1463) and peaks at 2θ of 23.15°, 33.02°, 36.18°, 38.25°, 45.14°, 49.29°, 35.14° and 65.89° correspond to (112), (222), (123), (004), (233), (134), (044) and (226) planes, respectively. The synthesized materials are found to be highly crystalline, indicated by the sharp diffraction peaks as shown in Fig. 1. The morphology of both materials was observed by SEM. A hexagonal plate-like morphology was observed for $Na_{2/3}MnO_2$ and the average particle size is found to be 2.273 μm as shown in Fig. 2a. On the other hand, agglomerated particles were found in case of Mn_2O_3 (Fig. 2c). The EDX pattern with atomic% of Mn (38.85%) and O (61.15%) in Fig. 2c clearly indicates the formation of Mn_2O_3. In TEM, the bright-field image (Fig. 3a) again clearly shows the platelet-like morphology of $Na_{2/3}MnO_2$ whereas the selected area electron diffraction shows the crystalline nature of the sample (Fig. 3b). The high-resolution TEM shows fringes with an interplanar spacing of about 0.428 nm corresponding to the (002) plane of hexagonal $Na_{2/3}MnO_2$.

The cyclic voltammograms (CVs) of $Na_{2/3}MnO_2$ were carried out at 10 mV s^{-1} in order to find the suitable potential range where it exhibits the capacitance properties. Rectangular-shaped CV is an indication of ideal double-layer capacitance property whereas CVs with redox peaks indicate the pseudocapacitance property. A pair of redox peaks at 0.58 V and 0.40 V during anodic and cathodic sweeps, respectively, are

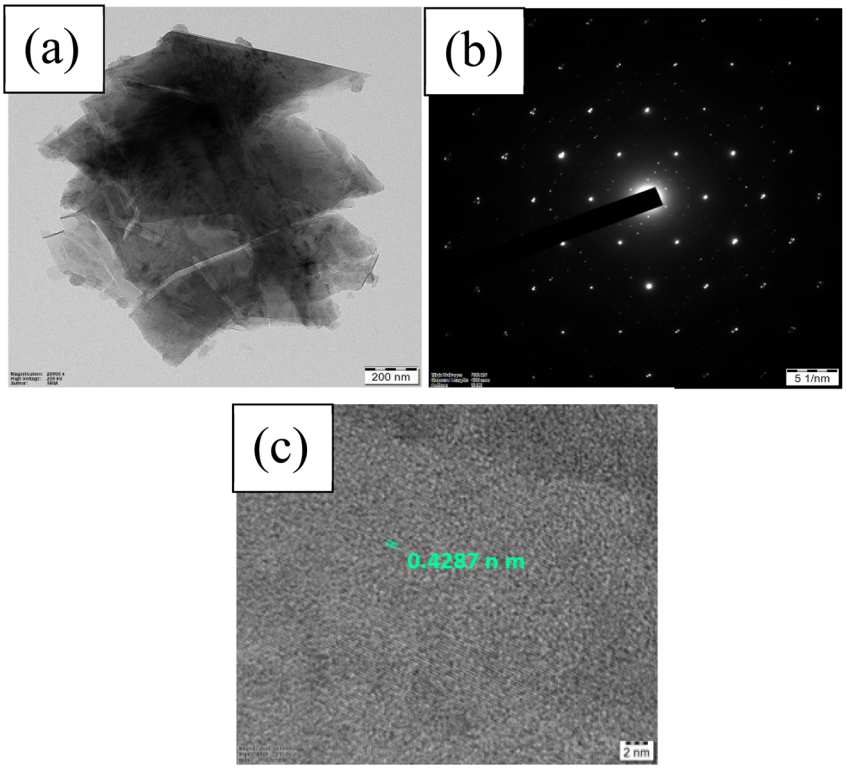

Fig. 3 TEM results of $Na_{2/3}MnO_2$ showing (a) bright-field image, (b) selected area electron diffraction (SAED) pattern, (c) HRTEM images of $Na_{2/3}MnO_2$ synthesized by hydrothermal method and annealed at 900 °C.

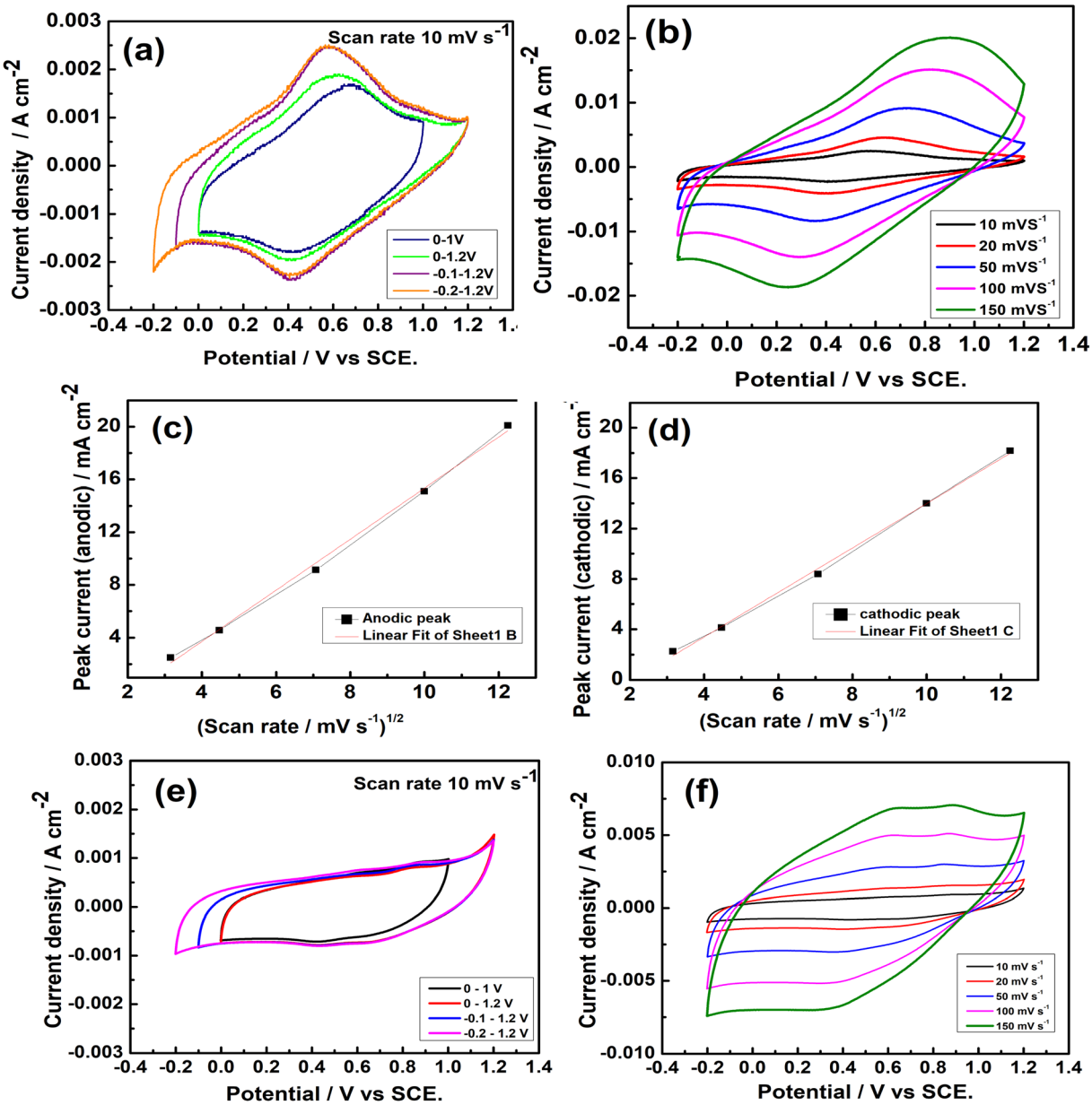

Fig. 4 (a) Cyclic voltammetry (CV) of $Na_{2/3}MnO_2$ in different potential ranges in an aqueous solution of 1.0 M Na_2SO_4, (b) CVs of $Na_{2/3}MnO_2$ at different scan rates in −0.2–1.2 V *vs.* SCE, (c) anodic peak current *vs.* square root of scan rate, (d) cathodic peak current *vs.* square root of scan rate, (e) CVs of Mn_2O_3 in different potential ranges in an aqueous solution of 1.0 M Na_2SO_4, (f) CVs of Mn_2O_3 at different scan rates in the potential range of −0.2–1.2 V *vs.* SCE.

clearly observed in the CVs measured (Fig. 4a) in the potential range of −0.2–1.2 V, indicating the pseudo-capacitance of $Na_{2/3}MnO_2$ in a wide potential range. The CVs were repeated at different sweep rates in the potential range of −0.2 to 1.2 V *vs.* SCE (Fig. 4b). Both the anodic and cathodic peak currents are found to increase with an increase in the sweep rate, indicating a diffusion-controlled electrode process. The peak currents were plotted against the square root of sweep rates, which is found to be linear (Fig. 4c and d). From the slope of these plots, the diffusion coefficient of ions was calculated by using the Randles–Sevcik equation:

$$I_p = 0.4463(nFD/RT)^{1/2}ACv^{1/2} \quad (1)$$

where I_p is the peak current, n is the number of electrons transferred in a redox reaction, F is the Faraday's constant, R is the universal gas constant, T is the absolute temperature, A is the working electrode area (cm^2), C is the molar concentration of the redox-active species (mol cm^{-3}), D is the diffusion coefficient ($cm^2\ s^{-1}$), v is the scan rate ($V\ s^{-1}$). The diffusion coefficient corresponding to anodic and cathodic processes are calculated and found to be $5.1943 \times 10^{-8}\ cm^2\ s^{-1}$ and $1.7570 \times 10^{-7}\ cm^2\ s^{-1}$, respectively.[59] In the case of Mn_2O_3, the CVs were found to be mostly rectangular with indistinct peaks when

measured at 10 mV s^{-1} in the potential range of −0.2–1.2 V, and the CVs were found to be symmetric without deviating from the rectangular shape with increased scan rates (Fig. 4e and f), similar to the previous report.[60]

Galvanostatic charge–discharge (GCD) cycling is widely used to determine the SC of various electrode materials. The galvanostatic charge–discharge of $Na_{2/3}MnO_2$ and Mn_2O_3 was carried out at 0.4 A g^{-1} in various potential ranges of 0–1.0, 0–1.2 and −0.2–1.2 V, which is shown in Fig. 5. The specific capacitances (SC) were evaluated by using the equation:

$$SC = I \times t/m(\Delta V) \quad (2)$$

where I is the current and (I/m) is the specific current, t is the charge/discharge time and ΔV is the operating voltage *vs.* SCE. It can be seen that the time taken for the charge/discharge for $Na_{2/3}MnO_2$ is higher, indicating the higher specific capacitance of $Na_{2/3}MnO_2$ over Mn_2O_3. The specific capacitances of $Na_{2/3}MnO_2$ and Mn_2O_3 were found to be 249, 226, 234 and 98.8, 102.3, 115.1 F g^{-1} at 0.4 A g^{-1} in the potential ranges of 0–1.0, 0–1.2 and −0.2–1.2 V, respectively. Thus, $Na_{2/3}MnO_2$ exhibits better capacitance property as compared to that of Mn_2O_3 synthesized by following the same hydrothermal method. These SCs of $Na_{2/3}MnO_2$ are found to be higher than that of Na_xMnO_2 in an aqueous Na_2SO_4 solution already reported.[32–35] It should be noted that hydrothermally synthesized MnO_2 at 140 °C for 6 h exhibited a SC of only 193 F g^{-1} in 1.0 M Na_2SO_4 aqueous solution.[61] Also, SCs in the range of 72–168 F g^{-1} were reported for MnO_2 synthesized by the hydrothermal method.[62] Thus, this study clearly indicates the higher SC of hydrothermally synthesized $Na_{2/3}MnO_2$ over MnO_2 and Mn_2O_3 when studied in an aqueous solution of Na_2SO_4.

The GCD cycling of $Na_{2/3}MnO_2$ and Mn_2O_3 was carried out at different specific currents, the variation of potential w.r.t. time in the wide potential range of −0.2–1.2 V (Fig. 6a and b) and the plot of SC against the specific currents are shown in Fig. 6c. The

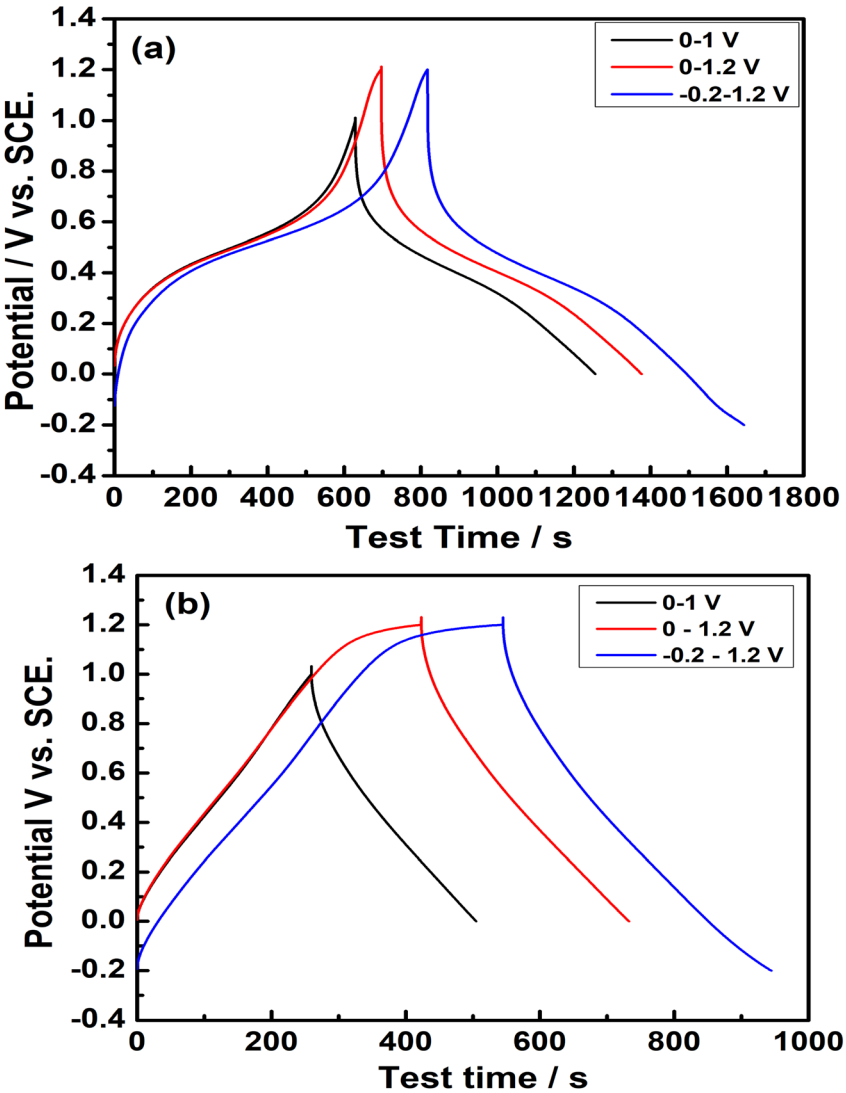

Fig. 5 Galvanostatic charge–discharge cycling of (a) $Na_{2/3}MnO_2$, (b) Mn_2O_3 at a current density of 0.4 A g^{-1} in different potential ranges *vs.* SCE in an aqueous solution of 1.0 M Na_2SO_4.

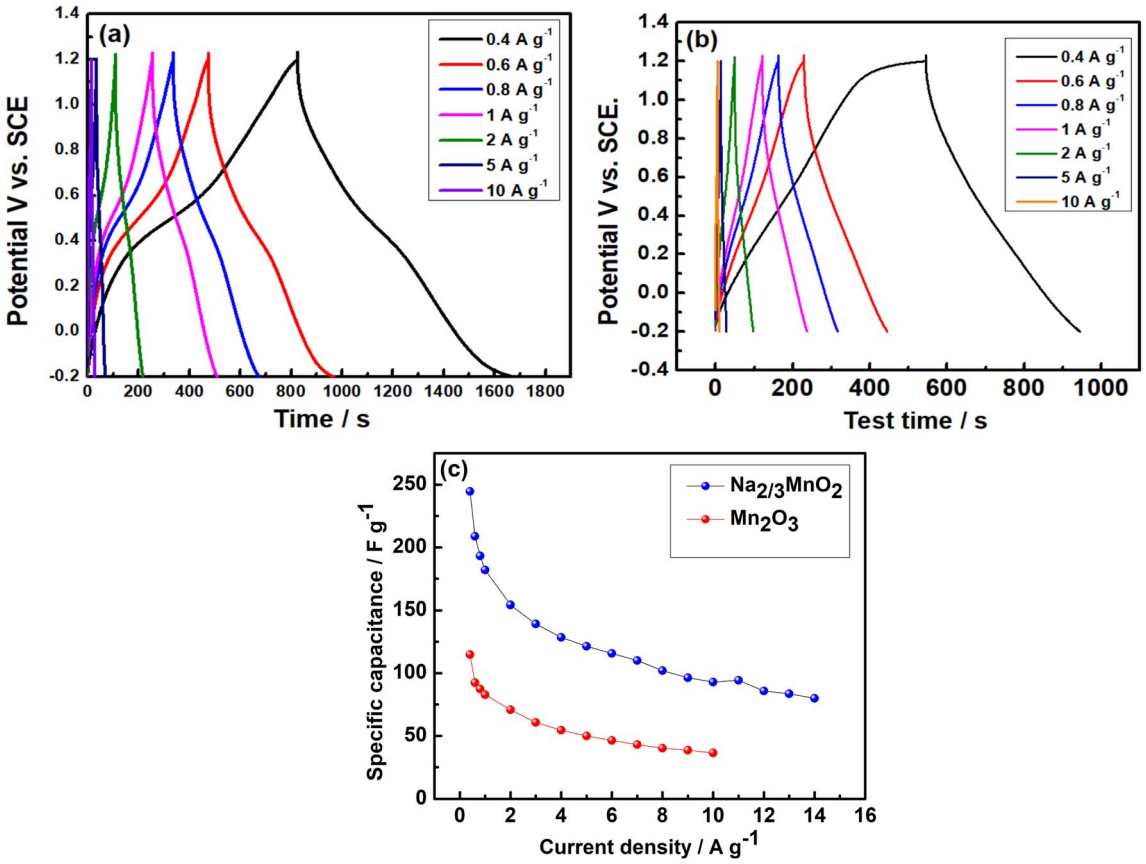

Fig. 6 Galvanostatic charge–discharge cycling at various specific currents for (a) $Na_{2/3}MnO_2$, (b) Mn_2O_3, (c) plot of specific capacitances of $Na_{2/3}MnO_2$ and Mn_2O_3 *vs.* specific currents in the potential range of −0.2 to 1.2 V *vs.* SCE.

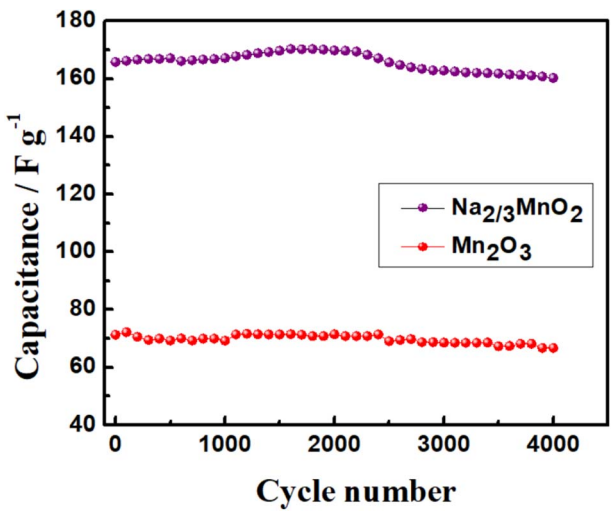

Fig. 7 Cycling stability of $Na_{2/3}MnO_2$ and Mn_2O_3 at a specific current of 2.0 A g^{-1} in the potential range of −0.2 to 1.2 V *vs.* SCE in an aqueous solution of 1.0 M Na_2SO_4.

SC decreased upon an increase of the specific current in both cases, *i.e.*, for $Na_{2/3}MnO_2$ about 160 F g^{-1} when cycled at 2 A g^{-1} and about 90 F g^{-1} at 10 A g^{-1} and for Mn_2O_3, it was about 70.8 F g^{-1} when cycled at 2 A g^{-1} and about 36.4 F g^{-1} at 10 A g^{-1}. Thus, the SC decreased for both samples with an increase in current, which can be due to the decreased utilization of active mass at high currents. However, this result indicates the higher rate capability of $Na_{2/3}MnO_2$ over Mn_2O_3.

In order to evaluate the long-term cycling stability of $Na_{2/3}MnO_2$ and Mn_2O_3, the galvanostatic charge–discharge cycling was carried out at 2.0 A g^{-1} in the potential range of −0.2–1.2 V for about 4000 cycles, which is shown in Fig. 7. The initial SC of $Na_{2/3}MnO_2$ was found to be 165 F g^{-1}, which increased gradually to a value of about 170 F g^{-1} during initial 1600 cycles and then started to decrease. Finally, a SC of about 160 F g^{-1} was obtained after the completion of 4000 cycles. Thus, this study clearly indicated the long-term cycling stability of $Na_{2/3}MnO_2$ in 1.0 M aqueous Na_2SO_4 electrolyte. In the case of Mn_2O_3, an initial SC of 71 F g^{-1} was obtained at 2.0 A g^{-1} when cycled in the same potential range, which decreased to 66 F g^{-1} after 4000 cycles. Thus, this result clearly indicates the importance of pre-sodiation in the improved capacitance properties of manganese-based oxides.

3.1 Performance of $Na_{2/3}MnO_2$||AC asymmetric capacitor

Considering the better capacitance properties of $Na_{2/3}MnO_2$ over Mn_2O_3, we tried to evaluate its performance in an asymmetric capacitor. In order to assemble an asymmetric capacitor with activated carbon (AC) as the negative electrode, the

capacitance property of AC was evaluated in 1.0 M aqueous Na_2SO_4 electrolyte. The CVs of AC were recorded in various potential ranges, whereas the GCD of AC was measured in the potential range of 0–(−0.8 V) *vs.* SCE. AC shows a rectangular-shaped CV without any redox activity, indicating its ideal double-layer capacitive property (Fig. S1†). A SC of about 250 F g^{-1} was obtained from the GCD of AC at 0.5 A g^{-1} (Fig. S1(b)†). Thus, in the three-electrode cell with Pt as the auxiliary electrode, both $Na_{2/3}MnO_2$ and AC exhibited high specific capacitances of 234 and 250 F g^{-1}, respectively, in the 1.0 M Na_2SO_4 electrolyte. However, in real two-electrode supercapacitors, AC is used as the negative electrode. Hence, we also performed the separate capacitance measurements of $Na_{2/3}MnO_2$ and AC using AC as the auxiliary and SCE as the reference electrode. The specific capacitances of $Na_{2/3}MnO_2$ and AC were found to be 80 and 60 F g^{-1}, respectively, in the potential ranges of 0–1.2 V and 0–(−0.8) V *vs.* SCE (Fig. S2†). It should be noted that, while high specific capacitances are reported in the literature using three-electrode cells, the specific capacitances reported for the electrochemical supercapacitors are usually less. Of course, the SC of the supercapacitor device should be around $(\frac{1}{4})$ th of the SC measured for the individual electrodes in three-electrode cells due to the series combination of both electrodes. The mass ratio of positive to negative electrode plays a significant factor in the evaluation of specific capacitance of an asymmetric capacitor. Wu *et al.* have studied the influence of this mass ratio on the performance of NiCo LDH‖ AC hybrid SC.[62] Taking into account the SCs of $Na_{2/3}MnO_2$ and AC and the potential windows of individual electrodes, the mass ratio was fixed at 1 : 1.4 by following the equation as reported earlier,[63,64]

$$m_+/m_- = SC_- \times \Delta E_-/SC_+ \times \Delta E_+ \quad (3)$$

The CVs were measured in different voltage ranges in order to get an appropriate voltage where it shows the capacitive property. A pair of redox peaks are clearly visible in the CVs, indicating the pseudocapacitive properties of the asymmetric supercapacitor, as shown in Fig. 8. It can be seen that the supercapacitor can be cycled to 2.0 V without any sharp oxidation peak at high voltages (Fig. 8). Asymmetric supercapacitors of MnO_2‖AC and $NaMnO_2$‖AC are already reported with working voltages of 2.0 V in aqueous electrolytes of Na_2SO_4.[36,63] The GCD was carried out at 0.1 A g^{-1} in order to evaluate the SC of this assembled supercapacitor device, which is shown in Fig. 8c. There is a linear variation of voltage with time, which indicates the capacitance property of the asymmetric supercapacitor within 2.0 V. A SC of about 37.7 F g^{-1} was obtained at 0.1 A g^{-1} based on the total masses of $Na_{2/3}MnO_2$ and AC with an operational voltage of 2.0 V. The GCD was carried out at different specific currents (Fig. 8d) in order to evaluate its power characteristic. A SC of about 16 F g^{-1} was obtained at 4.0 A g^{-1}, which indicates the high-power characteristic of this asymmetric supercapacitor.

The long-term cycling stability was performed by galvanostatic charge–discharge cycling at 0.8 A g^{-1} in 0–2.0 V. An initial SC of about 31.6 F g^{-1} was obtained, which increased to a value

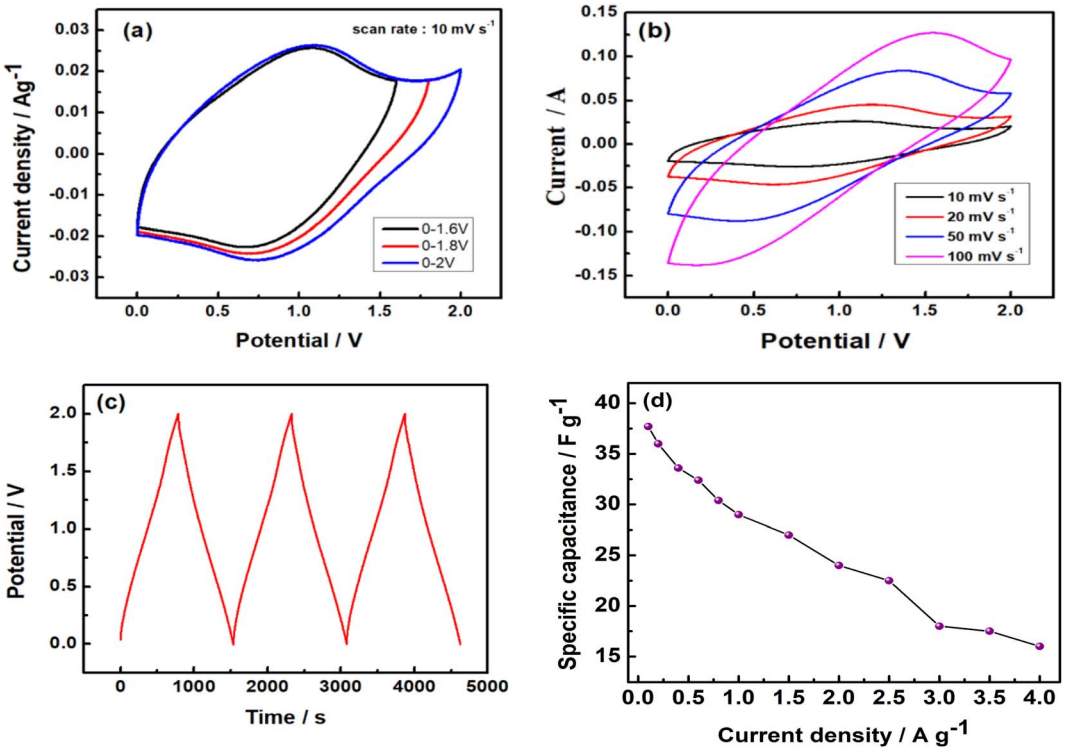

Fig. 8 (a) CVs of asymmetric $Na_{2/3}MnO_2$‖AC supercapacitor in different potential ranges, (b) CVs of the asymmetric supercapacitor at different scan rates, (c) galvanostatic charge–discharge cycles at a specific current of 0.1 A g^{-1}, and (d) rate capability tests at different specific currents in an aqueous solution of 1.0 M Na_2SO_4.

of 32.4 F g^{-1} during initial 1000 cycles and then stabilized even after 6000 cycles (Fig. 9). This result confirmed the long-term cycling stability of this asymmetric $Na_{2/3}MnO_2$||AC supercapacitor. Thus, $Na_{2/3}MnO_2$||AC can be a promising asymmetric supercapacitor considering the low cost and high abundance of Mn as well as Na.

The electrochemical impedance spectra (EIS) of the asymmetric capacitor were measured at open circuit potential during cycling, which is shown in Fig. 10. A semicircle at the high-frequency region corresponding to the parallel combination of charge transfer resistance and double-layer capacitance, followed by a linear spike at low frequency was observed in the Nyquist plots.[63] The intercepts at high frequency were found to be the same for the spectra measured after 1000 and 6000 cycles, indicating that the ohmic resistance (about 0.47 ohm) does not change upon cycling. Also, the charge transfer resistance (R_{ct}) at the electrode/electrolyte interface indicated by the diameter of semicircles decreased slightly upon cycling, which can support the slight increase in the SC of the asymmetric supercapacitor with cycling.

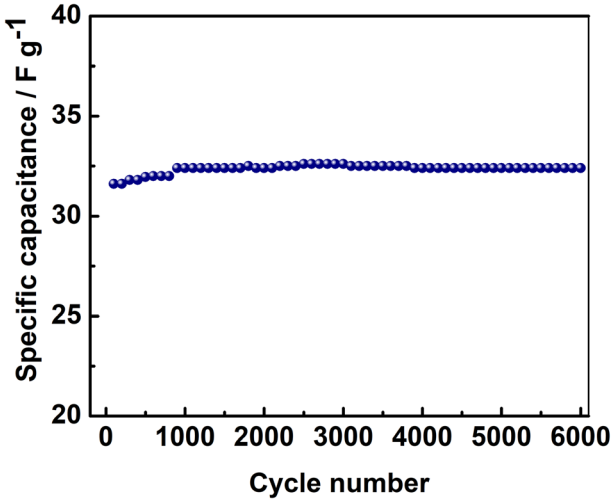

Fig. 9 Cycling stability of asymmetric $Na_{2/3}MnO_2$||AC supercapacitor at 0.8 A g^{-1} in an aqueous solution of 1.0 M Na_2SO_4.

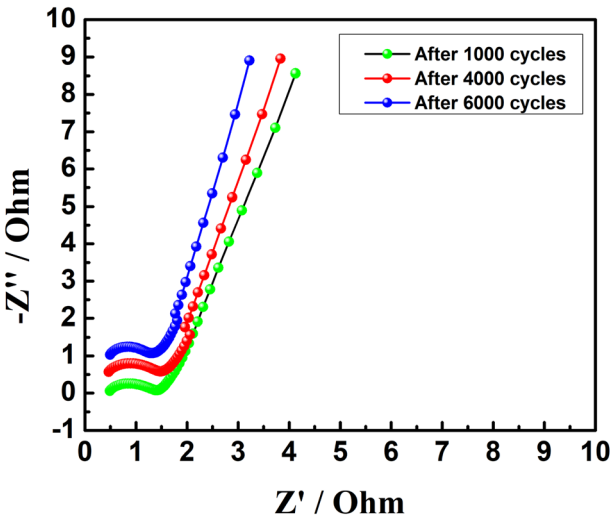

Fig. 10 Electrochemical impedance spectra (EIS) of asymmetric $Na_{2/3}MnO_2$||AC supercapacitor measured at open circuit potential during extensive cycling in an aqueous solution of 1.0 M Na_2SO_4.

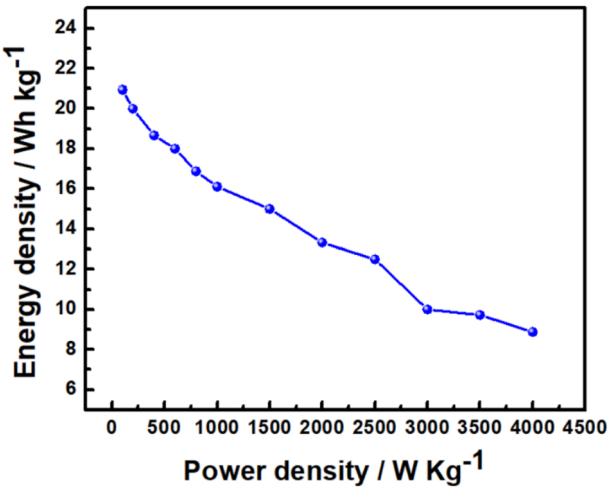

Fig. 11 Ragone plot of asymmetric $Na_{2/3}MnO_2$||AC supercapacitor in an aqueous solution of 1.0 M Na_2SO_4.

3.2 Calculation of energy and power density

Energy density and power density are the important characteristic features of a supercapacitor. The energy density (E) and power density (P) of this asymmetric capacitor were evaluated by using equations:

$$E = \frac{1}{2}CV^2 \quad (4)$$

$$P = \frac{1}{2}VI \quad (5)$$

where C is SC, V is the voltage and I is the charge–discharge current, plotted as Ragone plot in Fig. 11. An energy density of 20.9 W h kg^{-1} is obtained for this asymmetric supercapacitor, which is comparable with the reported energy density of 8–20 W h kg^{-1} for MnO_2 and $NaMnO_2$-based asymmetric supercapacitors.[36,48,63,65] It should be noted that symmetric capacitors based on AC||AC can provide an energy density of 5–6 W h kg^{-1} in aqueous electrolytes, because of low voltage. Thus, the asymmetric supercapacitor based on an aqueous electrolyte exhibits a higher energy density than the symmetric AC supercapacitors. A maximum power density of 4 kW kg^{-1} is achieved at the specific current of 4.0 A g^{-1}.

4. Conclusions

In this study, P2-$Na_{2/3}MnO_2$ and Mn_2O_3 are synthesized by a hydrothermal method followed by annealing at 900 °C for 12 h. A SC of 234 F g^{-1} was obtained for $Na_{2/3}MnO_2$ whereas it was only 115 F g^{-1} for Mn_2O_3 when cycled at a specific current of 0.4 A g^{-1} in 1.0 M aqueous Na_2SO_4 electrolyte. The specific

capacitance of the asymmetric $Na_{2/3}MnO_2$||AC supercapacitor slightly increased from 31.6 to 32.4 F g^{-1} when cycled at a specific current of 0.8 A g^{-1} during initial 1000 cycles and then stabilized even after 6000 cycles within 2.0 V, indicating its remarkable cycling stability. The electrochemical impedance study indicated that the charge transfer resistance did not change significantly upon extensive cycling, thus supporting the cycling stability of the asymmetric $Na_{2/3}MnO_2$||AC supercapacitor. Additionally, the asymmetric supercapacitor exhibited an energy density of 20.9 W h kg^{-1} and a power density of 4 kW kg^{-1}. Thus, the asymmetric $Na_{2/3}MnO_2$||AC supercapacitor can be very promising considering the low cost and environmental friendliness of Mn-based oxides as well as that of Na_2SO_4 electrolyte.

Author contributions

Aneesh Anand and P. K. Nayak conceptualized the work. Aneesh synthesized the sample and performed the experiments and wrote the original draft, which was reviewed and edited by P. K. Nayak.

Conflicts of interest

There are no conflicts of interest to declare.

Acknowledgements

The author Aneesh Anand thanks to the SRM Institute of Science and Technology (SRMIST) for providing the SRM Fellowship and all the research facilities, including SRM-SCIF for structural measurements. P. K. Nayak is grateful for the partial support within SRG funded by SERB, India.

References

1 X. Zhao, Y. Zhang, Y. Yang and H. Wei, *Batteries Supercaps*, 2019, **2**, 899–917.
2 H. B. Li, M. H. Yu, F. X. Wang, P. Liu, Y. Liang, J. Xiao, C. X. Wang, Y. X. Tong and G. W. Yang, *Nat. Commun.*, 2013, **4**, 1894–1989.
3 N. Hu, L. Huang, W. Gong and P. K. Shen, *ACS Sustainable Chem. Eng.*, 2018, **6**, 16933–16940.
4 K. Xu, J. Yang, S. Li, Q. Liu and J. Hu, *Mater. Lett.*, 2017, **187**, 129–132.
5 A. Ray, A. Roya, M. Ghosh, J. A. Ramos-Ramón, S. Saha, U. Pal, S. K. Bhattacharya and S. Das, *Appl. Surf. Sci.*, 2019, **463**, 513–525.
6 M. Winter and R. J. Brodd, *Chem. Rev.*, 2004, **104**, 4245–4269.
7 X. Zheng, L. Miao, Z. Song, W. Du, D. Zhu, Y. Lv, L. Li, L. Gan and M. Liu, *J. Mater. Chem. A*, 2022, **10**, 611–621.
8 Z. Song, L. Miao, L. Ruhlmann, Y. Lv, D. Zhu, L. Li, L. Gan and M. Liu, *Adv. Funct. Mater.*, 2022, **32**, 2208049–2208059.
9 L. Li, H. Hu and S. Ding, *Inorg. Chem. Front.*, 2018, **5**, 1714–1720.
10 M. Dakshana, S. Meyvel, M. Malarvizhi, P. Sathya, R. Ramesh, S. Prabhu and M. Silambarasan, *Vacuum*, 2020, **174**, 109218–109228.
11 Z. Liu, L. Zhang, G. Xu, L. Zhang, D. Jia and C. Zhang, *RSC Adv.*, 2017, **7**, 11129–11134.
12 Q. Y. Li, Z. S. Li, L. Lina, X. Y. Wang, Y. F. Wang, C. H. Zhang and H. Q. Wang, *Chem. Eng. J.*, 2010, **156**, 500–504.
13 R. R. Rajagopal, L. S. Aravinda, R. Rajarao, B. R. Bhat and V. Sahajwalla, *Electrochim. Acta*, 2016, **211**, 488–498.
14 J. P. Zheng, P. J. Cygan and T. R. Jow, *J. Electrochem. Soc.*, 1995, **142**, 2699–2703.
15 Y. Liu, W. Zhao and X. Zhang, *Electrochim. Acta*, 2008, **53**, 3296–3304.
16 R. Warren, F. Sammoura, F. Tounsi, M. Sanghadasa and L. Lin, *J. Mater. Chem. A*, 2015, **3**, 15568–15575.
17 J. Zhang, J. Ma, L. L. Zhang, P. Guo, J. Jiang and X. S. Zhao, *J. Phys. Chem. C*, 2010, **114**, 13608–13613.
18 S. D. Dhas, P. S. Maldar, M. D. Patil, A. B. Nagare, M. R. Waikar, R. G. Sonkawade and A. V. Moholkar, *Vacuum*, 2020, **181**, 109646–109654.
19 H. Xiao, S. Yao, H. Liu, F. Qu, X. Zhang and X. Wu, *Prog. Nat. Sci.: Mater. Int.*, 2016, **26**, 271–275.
20 P. K. Nayak and N. Munichandraiah, *Mater. Sci. Eng., B*, 2012, **177**, 849–854.
21 M. Yang, K. Li and L. Xiao, *Mater. Sci. Eng., B*, 2021, **269**, 115173–115179.
22 H. B. Li, M. H. Yu, F. X. Wang, P. Liu, Y. Liang, J. Xiao, C. X. Wang, Y. X. Tong and G. W. Yang, *Nat. Commun.*, 2013, **4**, 1894–1900.
23 X. Xiong, D. Ding, D. Chen, G. Waller, Z. Wang and M. Liu, *Nano Energy*, 2015, **11**, 154–161.
24 T. E. Kibona, *J. Solid State Electrochem.*, 2020, **42**, 1587–1598.
25 X. Liu, S. Shi, Q. Xiong, L. Li, Y. Zhang, H. Tang, C. Gu, X. Wang and J. Tu, *ACS Appl. Mater. Interfaces*, 2013, **5**, 8790–8795.
26 T. Munawar, M. Shahid, N. Faisal, M. Sumaira, M. Muhammad, N. Ashiq and F. Iqbal, *Mater. Sci. Eng., B*, 2022, **284**, 115900–115911.
27 M. A. Yewale, R. A. Kadam, N. K. Kaushik, J. R. Koduru, N. B. Velhal, U. T. Nakate, A. A. Jadhavar, N. D. Sali and D. K. Shin, *Mater. Sci. Eng., B*, 2023, **287**, 116072–116083.
28 A. Cherusseri, N. Choudhary, K. S. Kumar, Y. Jung and J. Thomas, *Nanoscale Horiz.*, 2019, **4**, 840–858.
29 M. Abuali, N. Arsalani, I. Ahadzadeh and T. Nann, *Mater. Sci. Eng., B*, 2022, **276**, 115578–115590.
30 P. Yang, L. Feng, J. Hu, W. Ling, S. Wang, J. Shi, Z. Yang and F. Wang, *ChemElectroChem*, 2019, **6**, 1–9.
31 M. Barazandeh and S. H. Kazemi, *Sci. Rep.*, 2022, **12**, 4628–4640.
32 T. Xiong, W. Siang, V. Lee and J. Xue, *ACS Appl. Energy Mater.*, 2018, **1**, 5619–5626.
33 N. Jabeen, A. Hussain, Q. Xia, S. Sun, J. Zhu and H. Xia, *Adv. Mater.*, 2017, **29**, 1700804–1700812.
34 N. Karikalan, C. Karuppiah, S. Chen, M. Velmurugan and P. Gnanaprakasam, *Chem. - Eur. J.*, 2017, **23**, 2379–2386.
35 B. H. Zhang, Y. Liu, Z. Chang, Y. Q. Yang, Z. B. Wen, Y. P. Wu and R. Holze, *J. Power Sources*, 2014, **253**, 98–103.

36 Q. T. Qu, Y. Shi, S. Tian, Y. H. Chen, Y. P. Wu and R. Holze, *J. Power Sources*, 2009, **194**, 1222–1225.
37 V. Subramanian, H. Zhu, R. Vajtai, P. M. Ajayan and B. Wei, *J. Phys. Chem. B*, 2005, **109**, 20207–20214.
38 P. K. Nayak and N. Munichandraiah, *Microporous Mesoporous Mater.*, 2011, **143**, 206–214.
39 Y. Li, H. Xie, J. Wang and L. Chen, *Mater. Lett.*, 2011, **65**, 403–405.
40 T. Cottineau, M. Toupin, T. Delahaye, T. Brousse and D. Belanger, *Appl. Phys. A*, 2006, **82**, 599–606.
41 M.-S. Wu, *Appl. Phys. Lett.*, 2005, **87**, 153102–153104.
42 C. Wei, H. Pang, B. Zhang, Q. Lu, S. Liang and F. Gao, *Sci. Rep.*, 2013, **3**, 2193–2197.
43 J. R. Choi, J. Lee, G. Yang, Y. J. Heo and S. J. Park, *Catalysts*, 2020, **10**, 256–265.
44 P. Murovhi, D. J. Tarimo, K. O. Oyedotun and N. Manyala, *J. Energy Storage*, 2020, **32**, 101797–101807.
45 Z. Fan, J. Ren, F. Zhang, T. Gu, S. Zhang, R. P. Ren and Y. K. Lv, *J. Mater. Sci.*, 2022, **57**, 1281–1290.
46 Q. Z. Zhang, D. Zhang, Z. C. Miao, X. L. Zhang and S. L. Chou, *Small*, 2018, **14**, 1702883–1702897.
47 M. S. Hong, S. H Lee and S. W. Kim, *Solid State Lett.*, 2002, **5**, A227–A230.
48 S. Xu, T. Wan, K. Zhou, G. Zhu, Z. He, H. Huang, T. Zhou, W. Mao, J. Wu, S. Gong and Y. Qiao, *Mater. Res. Express*, 2020, **7**, 035508–035526.
49 X. Wang, W. S. Liu, X. Lu and P. S. Lee, *J. Mater. Chem.*, 2012, **22**, 23114–23119.
50 J. Zhang, F. Liu, J. P. Cheng and X. B. Zhang, *ACS Appl. Mater. Interfaces*, 2015, **7**, 17630–17640.
51 G. Godillot, P.-L. Taberna, B. Daffos, P. Simon, C. Delmas, L. G. Demourgues and G. Godillot, *J. Power Sources*, 2016, **331**, 277–284.
52 S. Pappu, K. Nanaji, S. Mandati, T. N. Rao, S. K. Martha and S. V. Bulusu, *Batteries Supercaps*, 2020, **3**, 1209–1219.
53 A. Konarov, H. J. Kim, N. Voronina, Z. Bakenov and S. T. Myung, *ACS Appl. Mater. Interfaces*, 2019, **11**, 28928–28933.
54 Z. Zhou, J. Li, Z. Luo, Z. He, J. Zheng, Y. Li, J. Mao, K. Dai, C. Yan and Z. Sun, *Ionics*, 2021, **27**, 5187–5196.
55 S. Kumakura, Y. Tahara, S. Sato, K. Kubota and S. Komaba, *Chem. Mater.*, 2017, **29**, 8958–8962.
56 S. Kumakura, Y. Tahara, K. Kubota, K. Chihara and S. Komaba, *Angew. Chem.*, 2016, **128**, 12952–12955.
57 C. Ke, F. Fu, J. Zheng and W. Yang, *Ionics*, 2019, **26**, 727–734.
58 P. K. Nayak, L. Yang, K. Pollok, F. Langenhorst, L. Wondraczek and P. Adelhelm, *Batteries Supercaps*, 2019, **2**, 104–111.
59 N. S. Neghmouche and T. Lanez, *Recent Trends in Physical Chem.: An International J*, 2013, **1**, 1–3.
60 W. Li, J. Shao, Q. Liu, X. Liu, X. Zhou and J. Hu, *Electrochim. Acta*, 2015, **157**, 108–114.
61 P. K. Nayak and N. Munichandraiah, *J. Solid State Electrochem.*, 2012, **16**, 2739–2749.
62 Q. Qin, D. Ou, C. Ye, L. Chen, B. Lan, J. Yan and Y. Wu, *Electrochim. Acta*, 2019, **305**, 403–415.
63 V. Khomenko, E. R. Piñero and F. Béguin, *J. Power Sources*, 2006, **153**, 183–190.
64 R. Mohanty, G. Swain, K. Parida and K. Parida, *J. Alloys Compd.*, 2022, **919**, 165753–165765.
65 T. Cottineau, M. Toupin, T. Delahaye, T. Brousse and D. Belanger, *Appl. Phys. A*, 2006, **82**, 599–606.